JB
Journals.ASM.org

myo-Inositol and D-Ribose Ligand Discrimination in an ABC Periplasmic Binding Protein

Julien Herrou,[a] Sean Crosson[a,b]

Department of Biochemistry and Molecular Biology, University of Chicago, Chicago, Illinois, USA[a]; The Committee on Microbiology, University of Chicago, Chicago, Illinois, USA[b]

The periplasmic binding protein (PBP) IbpA mediates the uptake of *myo*-inositol by the IatP-IatA ATP-binding cassette transmembrane transporter. We report a crystal structure of *Caulobacter crescentus* IbpA bound to *myo*-inositol at 1.45 Å resolution. This constitutes the first structure of a PBP bound to inositol. IbpA adopts a type I PBP fold consisting of two α-β lobes that surround a central hinge. A pocket positioned between the lobes contains the *myo*-inositol ligand, which binds with submicromolar affinity (0.76 ± 0.08 μM). IbpA is homologous to ribose-binding proteins and binds D-ribose with low affinity (50.8 ± 3.4 μM). On the basis of IbpA and ribose-binding protein structures, we have designed variants of IbpA with inverted binding specificity for *myo*-inositol and D-ribose. Five mutations in the ligand-binding pocket are sufficient to increase the affinity of IbpA for D-ribose by 10-fold while completely abolishing binding to *myo*-inositol. Replacement of *ibpA* with these mutant alleles unable to bind *myo*-inositol abolishes *C. crescentus* growth in medium containing *myo*-inositol as the sole carbon source. Neither deletion of *ibpA* nor replacement of *ibpA* with the high-affinity ribose binding allele affected *C. crescentus* growth on D-ribose as a carbon source, providing evidence that the IatP-IatA transporter is specific for *myo*-inositol. This study outlines the evolutionary relationship between ribose- and inositol-binding proteins and provides insight into the molecular basis upon which these two related, but functionally distinct, classes of periplasmic proteins specifically bind carbohydrate ligands.

Cellular growth in chemically complex environments requires multiple systems for the transport of metabolic substrates. In the bacterial kingdom, specific transmembrane transporters facilitate the uptake of diverse molecular substrates as energy sources and anabolic building blocks. Three families of transporters have been broadly characterized: (i) the ATP-binding cassette (ABC) transporters (1, 2), (ii) the tripartite ATP-independent periplasmic (TRAP) transporters (3, 4), and (iii) the tripartite tricarboxylate (TTT) transporters (5). These transporters are known to recruit periplasmic binding proteins (PBPs) that bind a specific ligand(s) with high affinity (5–7). PBPs are widespread in Gram-negative bacteria but vary significantly both at the primary sequence level and in the types of ligands they bind. The primary functional roles of PBPs are nutrient transport and environmental sensing (6, 8–12). In the case of nutrient transport, the PBP undergoes a transition upon substrate binding that typically involves open-to-closed conformational changes. The PBP then docks with the transmembrane transporter and releases the substrate for carriage across the membrane and into the cell. Depending on the transporter class, the substrate translocation process is driven by proton motive force, electrochemical gradients, or ATP hydrolysis (7, 13).

The freshwater alphaproteobacterium *Caulobacter crescentus* transports and metabolizes a range of organic nutrients, including the abundant environmental carbohydrate *myo*-inositol (14). Inositol is an important molecule in many microbial ecosystems; inositol and its derivatives can serve as antioxidants, as cell membrane components, as osmolytes, and as carbon storage units in bacteria and archaea (15, 16). It is also a carbon and energy source for many bacterial species (17–21); in its phosphorylated forms, inositol can serve as a phosphorus source (22, 23).

In *Caulobacter*, cellular utilization of *myo*-inositol requires an ABC transporter that consists of the PBP IbpA, the transmembrane permease IatP, and the ABC IatA (14). Once *myo*-inositol has entered the cell, enzymes encoded from a conserved gene cluster (*iolCDEBA-idhA*) catalyze its stepwise degradation, yielding dihydroxyacetone phosphate, acetyl coenzyme A, NADH, and NADPH (17, 24, 25, 26, 27). The transcriptional regulatory protein IolR inhibits the expression of the transporter operon and the catabolic enzymes in *C. crescentus* (14) (Fig. 1) and in related alphaproteobacteria (14, 28).

In an effort to define the molecular basis of *myo*-inositol binding specificity in the *C. crescentus* ABC transporter system, we have solved the crystal structure of IbpA bound to *myo*-inositol at 1.45 Å resolution. To our knowledge, this constitutes the first structure of a PBP bound to any form of inositol. IbpA adopts a classic type I clam-like PBP fold (6, 29), with α-β globular lobes separated by a central three-segment hinge. The two lobes and the hinge surround a central ligand-binding cavity, where the six-carbon carbohydrate *myo*-inositol (*cis*-1,2,3,5-*trans*-4,6-cyclohexanehexol) is bound with high affinity (K_d = 760 ± 80 nM). IbpA has sequence and structural features in common with the ribose-binding proteins (RBPs) (30–33) and binds the 5-carbon carbohydrate α-D-ribose [(3*R*,4*S*,5*R*)-5-(hydroxymethyl)oxolane-2,3,4-triol], with low affinity (K_d = 50.8 ± 3.4 μM). A phylogenetic analysis of IbpA and ribose-binding PBP sequences reveals that *C. crescentus* IbpA occupies an intermediate evolutionary position between *myo*-inositol-binding PBPs and ribose-binding PBPs. Combining

Received 25 January 2013 **Accepted** 12 March 2013
Published ahead of print 15 March 2013
Address correspondence to Sean Crosson, scrosson@uchicago.edu.
Supplemental material for this article may be found at http://dx.doi.org/10.1128/JB.00116-13.

doi:10.1128/JB.00116-13

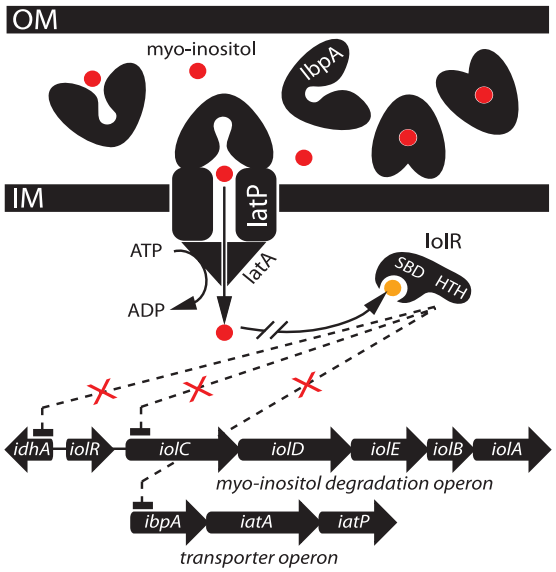

FIG 1 Model of *myo*-inositol uptake and catabolism in *Caulobacter*. When present in the environment, *myo*-inositol is bound by the PBP IbpA, which contacts the transmembrane transporter IatP and delivers the sugar to the cytoplasmic space. Translocation of *myo*-inositol (red circle) from the periplasm to the cytoplasm is energized by the hydrolysis of ATP by the ABC protein IatA. *myo*-Inositol in the cytoplasm is then catabolized, and the late pathway intermediate 2-keto-5-deoxy-D-gluconate-6-phosphate (orange circle) functions as the inducer of the *iol* genes by inhibiting the IolR response regulator through a direct interaction with its sugar-binding domain (SBD). Genes (*idhA*, *iolC*, and *ibpA*) normally repressed in the absence of *myo*-inositol are transcribed, facilitating the metabolism of *myo*-inositol. OM, outer membrane; IM, inner membrane.

primary sequence data with our IbpA crystal structure, we have engineered a variant cavity mutant (CM), $IbpA_{CM2}$, that binds ribose with high affinity (4.9 ± 1.2 μM) but does not bind *myo*-inositol. This switch in carbohydrate binding specificity required a total of five mutations that modify specific polar contacts with the carbohydrate and alleviate the steric clash between carbohydrate-interacting side chains. Replacement of the wild-type *ibpA* allele on the *C. crescentus* chromosome with $ibpA_{CM2}$ completely blocked cellular growth in *myo*-inositol minimum medium and did not confer improved growth on D-ribose. Moreover, strains in which the permease (*iatP*) or ATPase (*iatA*) transporter components were deleted exhibited wild-type growth rates on D-ribose as the sole carbon source. Thus, the IbpA-IatP-IatA ABC transporter system specifically transports *myo*-inositol and not D-ribose under the culture conditions tested.

MATERIALS AND METHODS

Construction of expression plasmids. The sequence encoding residues 39 to 327 of *myo*-inositol-binding protein (IBP; *ibpA* gene number *CC_0859*) was amplified by PCR from *C. crescentus* NA1000 genomic DNA. The PCR product was isolated by agarose gel extraction (Omega Biotek), cloned into the PCR-Blunt II-TOPO vector (Invitrogen), and sequenced. *ibpA* was cut as an NdeI-HindIII fragment from the TOPO vector and ligated into the corresponding sites of pET28c (Novagen). The resulting plasmid encodes IbpA(39-327) with an N-terminal 6×His tag. Mutations in the IbpA ligand-binding cavity were successively introduced by overlapping PCR (for the sequences of the primers used, see Table S1 in the supplemental material). Two different sets of mutations were introduced, corresponding to IbpA CM1 ($IbpA_{CM1}$: Q49N, D169I, S174A, and S203F) and IbpA CM2 ($IbpA_{CM2}$: Q49N, N168G, D169I, S174A, and S203F).

IbpA expression and purification. Recombinant IbpA proteins (wild-type IbpA, $IbpA_{CM1}$, and $IbpA_{CM2}$) were expressed in *E. coli* Rosetta(DE3)pLysS (Novagen) (for strain numbers and characteristics, see Table S2 in the supplemental material). A 50-ml overnight LB medium culture supplemented with 50 μg/ml kanamycin ($LB\text{-}Kan_{50}$) was used to inoculate 1 liter of $LB\text{-}Kan_{50}$; this culture was incubated at 37°C in a rotary shaker at 220 rpm. Transcription of recombinant *ibpA* was induced at an optical density at 600 nm (OD_{600}) of 0.8 by adding 1 mM isopropyl-β-D-thiogalactopyranoside (IPTG). After 4 h of induction, the cells were harvested by centrifugation at 12,000 × *g* for 20 min at 4°C. Cell pellets were resuspended in 30 ml of lysing/binding buffer (10 mM Tris [pH 7.4], 150 mM NaCl, 10 mM imidazole) supplemented with DNase I (Sigma-Aldrich) and phenylmethylsulfonyl fluoride (Sigma-Aldrich).

Cells were disrupted by three passages in a French pressure cell, and the cell debris was removed by centrifugation for 20 min at 25,000 × *g*. The supernatant was loaded onto a Ni^{2+} Sepharose affinity column (GE Life Sciences) pre-equilibrated with the binding buffer. Two washing steps were performed with 10 and 75 mM imidazole, followed by two elution steps with 200 mM and 1 M imidazole in the binding buffer. The protein solution was then dialyzed against 10 mM Tris (pH 7.4) and 150 mM NaCl buffer to remove the imidazole. All purification steps were carried out at 4°C. All concentrations were measured with a NanoDrop 1000 spectrophotometer (Thermo Scientific).

Crystallization of IbpA bound to *myo*-inositol. Initial attempts to phase the IbpA structure by molecular replacement failed because of problems with crystal pseudosymmetry. We produced selenium-labeled protein for experimental phase determination. IbpA was expressed in a defined medium containing selenomethionine as previously described (34). Purified wild-type SeMet-labeled IbpA was purified and concentrated with a centrifugal filter (3-kDa molecular mass cutoff; Amicon-Millipore). Protein purity was estimated to be 95% as assessed by 12% SDS-PAGE and staining with Coomassie brilliant blue. Initial crystallization screening was carried out by the sitting-drop vapor diffusion technique in 96-well microplates (Nunc). Trays were set up with a Mosquito robot (TTP LabTech) and commercial crystallization kits (Nextal-Qiagen). The drops were set up by mixing equal volumes (0.1 μl) of the protein and the precipitant solutions equilibrated against 75 μl of the precipitant solution. In all trials, the protein concentration was ~50 mg/ml (~1.6 mM) supplemented with 5 mM *myo*-inositol (Calbiochem, EMD Millipore). In approximately 1 week, small crystals appeared in condition 44 of the Classics Suite II crystallization kit (Qiagen). After manual refinement of the crystallization condition, the best crystals were obtained at 19°C with a crystallization solution containing 75 mM HEPES (pH 7.4), 25% (wt/vol) polyethylene glycol 3350, and 5 mM *myo*-inositol. All manual crystallization attempts were carried out by the hanging-drop vapor diffusion technique in 24-well plates (Hampton). Microseeding of pre-equilibrated drops with a cat whisker improved the shape, size, and quality of the crystals. The drops were set up by mixing equal volumes (3 μl) of the protein and the precipitant solutions equilibrated against 500 μl of the precipitant solution. Crystals grew to their final size in 7 to 10 days. Before flash freezing with liquid nitrogen, crystals were cryoprotected by soaking in a crystallization solution containing 30% glycerol and 5 mM β-mercaptoethanol.

Crystallographic data collection and data processing. Crystal diffraction was measured at a temperature of 100 K with a 1° oscillation range on beamline 21-ID-D (Life Sciences Collaborative Access Team, Advanced Photon Source, Argonne, IL); diffraction images were collected on a MAR Mosaic 300 detector. Diffraction images were processed with the HKL 2000 suite (35). Geometric refinement and examination of the scaled amplitudes revealed that the Se-Met IbpA crystals belong to monoclinic space group C2, with cell dimensions a = 83.1 Å, b = 34.9 Å, and c = 181.8 Å (β = 102.6°) (see Table 1).

Diffraction from a single Se-Met IbpA protein crystal was measured at

TABLE 1 Crystallographic data and refinement statistics

Parameter	Value(s)[e]
Data collection statistics	
Energy (keV)	12.66
Resolution range (Å)	19.9–1.45 (1.47–1.45)
No. of unique reflections	77,441
R_{merge}[a]	0.08
$\langle I\rangle/\langle s_I\rangle$ ratio	14.8 (2.0)
Avg % redundancy	4.2 (3.8)
Avg % completeness	99.0 (98.9)
Phasing statistics (19.9–1.45 Å),[b] figures of merit:	
Acentric	0.47
Centric	0.17
Overall	0.35
Refinement statistics	
Space group	C2
a, b, c (Å)	83.1, 34.9, 181.8
β (°)	102.6
R_{cryst}[c]	0.166
R_{free}[d]	0.188
$\langle B\rangle$ (Å^2)	16.9
RMSD of bond lengths (Å)	0.010
RMSD of bond angles (°)	1.321
Ramachandran analysis	
% Preferred	98.5
% Allowed	0.8
% Disallowed	0.7

[a] $R_{merge} = \Sigma_{hkl}\Sigma_i |I_i - \langle I\rangle|/\Sigma_{hkl}\Sigma_i I_i$. For all data, $I/\sigma(I) = >3$.
[b] Initial phases were determined by selenium Autosol SAD (see Materials and Methods).
[c] $R_{cryst} = \Sigma_{hkl} ||F_{obs}| - |F_{calc}||/\Sigma_{hkl} |F_{obs}|$ (includes all data).
[d] R_{free} uses 1,945 total reflections for cross-validation.
[e] The values in parentheses represent the highest-resolution shell.

an energy of 12.66 keV (0.979 Å), and the structure was phased from the resulting 1.45-Å data set by single-wavelength anomalous dispersion (36). Two IbpA monomers are in the asymmetric unit. Eighteen selenium sites (nine in each monomer) were located within the asymmetric unit by the Autosol SAD routine within the Phenix software suite (37). A preliminary IbpA structural model (R_{work} of 20%, R_{free} of 23%) was built *de novo* from the initial experimental, solvent-flattened maps by the AutoBuild routine and phenix.refine. This initial model was then manually examined and corrected; solvent addition and refinement of the structure were conducted iteratively with Coot (38) and phenix.refine (37). The final structural model was refined to an R_{work} of 16.6% and an R_{free} of 18.8%. Crystallographic data and refined model statistics are presented in Table 1.

Genetic manipulations and engineering of *C. crescentus* allelic-replacement strains. The chromosomal copy of the wild-type *ibpA* allele was replaced in the *C. crescentus* NA1000 (39) genetic background with two *ibpA* CM alleles ($ibpA_{CM1}$ and $ibpA_{CM2}$) by a double-recombination gene replacement strategy (40). Briefly, *ibpA* mutant alleles were cloned into suicide plasmid pNPTS138 (M. R. K. Alley, unpublished data), which carries the *nptI* gene for initial selection and the *sacB* gene for counterselection on sucrose. A *C. crescentus* NA1000 Δ*ibpA* strain (FC488) was transformed with pNPTS138-*ibpA* plasmids by electroporation, and single-crossover integrants were selected on peptone-yeast extract (PYE) kanamycin (25 μg/ml) agar plates. Counterselection for the second crossover and PCR screening to identify strains in which the wild-type allele was replaced with a mutant allele were carried out as described previously (41). See Tables S1 and S2 in the supplemental material for primer, plasmid, and strain information.

Cell growth assays. Wild-type and mutant strains of *C. crescentus* NA1000 were grown overnight in culture tubes containing 5 ml of PYE medium. After overnight growth, OD_{660}s were assessed. Bacteria were then harvested by centrifugation (20,000 × *g* for 1 min), and the pellets were washed three times with minimum medium (M2) and reharvested by centrifugation. The densities of cultures for growth rate assays were adjusted by resuspending the washed pellets in the appropriate volume of M2 medium. Equal volumes of the density-adjusted cultures were then used to inoculate (to an OD_{660} of 0.05) tubes containing 3 ml of M2 minimum medium supplemented with 0.2% (wt/vol) D-ribose (Sigma-Aldrich) or 0.2% (wt/vol) *myo*-inositol (Calbiochem). The growth kinetics of the different strains were measured by tracking the OD_{660} each day for 1 week. Each growth experiment was repeated three times.

ITC ligand biding assays. To ensure that the IbpA protein sample lacked ligand prior to the isothermal titration calorimetry (ITC) carbohydrate binding assays, purified wild-type and mutant IbpA proteins were extensively dialyzed against 2 liters of 10 mM Tris (pH 7.4)–150 mM NaCl buffer over 12 h; this dialysis procedure was serially repeated four times. We assume that after affinity chromatography and four serial 2-liter dialysis steps carried out across 4 days, random stray ligand obtained from *E. coli* lysate will be mostly lost. This assumption is based on typical microscopic dissociation rate constants of 1 to 100 s^{-1} for ligands bound to PBPs (42) and a low micromolar concentration of IbpA in the dialysis bag. However, it is possible that a small fraction of our sample had unknown ligand bound prior to the ITC measurements.

All samples (proteins and ligands) were degassed for 20 min prior to ITC measurements, and final sample dilutions were carried out by using the final dialysis buffer. Ligands were injected into a 200-μl sample cell containing 50 μM protein for the *myo*-inositol titrations and 100 μM protein for the D-ribose titrations. Concentrations of 1 and 10 mM *myo*-inositol were tested on wild-type IbpA (40 injections) and CM1 and CM2 IbpA mutants (20 injections), respectively. For D-ribose, a concentration of 10 mM was used for wild-type IbpA and $IbpA_{CM1}$ (40 and 20 injections, respectively). A concentration of 5 mM D-ribose was used for $IbpA_{CM2}$ titrations (40 injections). ITC was performed at 25°C with a 0.5-μl injection volume every 200 s. All ligands were titrated into ITC buffer alone, and the resulting heat of dilution was subtracted from each experimental curve. ITC was performed with an iTC_{200} microcalorimeter (MicroCal; GE Healthcare). Data were analyzed and fitted with Microcal Origin software. Each titration was performed three times.

CD spectroscopy. Overall folding and secondary structure of IbpA and mutant variants were assessed by circular dichroism (CD) spectroscopy. Prior to CD measurements, purified protein samples were dialyzed in a buffer containing 50 mM sodium phosphate (pH 7.4) and 50 mM NaCl. CD spectra from 180 to 260 nm were measured on an AVIV 202 CD spectrometer. Mean ellipticity units per residue (after buffer subtraction) were calculated for each spectrum, and data were analyzed with the K2D3 software (http://www.ogic.ca/projects/k2d3) to estimate protein secondary structure (43).

Sequence alignment and protein visualization methods. The Dali server (http://ekhidna.biocenter.helsinki.fi/dali_server/) (44) was used to align the IbpA structure with structures in the Protein Data Bank (PDB). Protein sequence alignments were carried out in ClustalW2 (http://www.ebi.ac.uk/Tools/msa/clustalw2/) (45) and shaded in Boxshade (http://www.ch.embnet.org/software/BOX_form.html). IbpA ribbon rendering, IbpA/RBP_{Tt} structural alignment, and ligand binding comparisons were carried out in PyMOL (version 1.3; Schrödinger, LLC). The PDBsum server (http://www.ebi.ac.uk/thornton-srv/databases/pdbsum/Generate.html) was used to define the molecular interaction map between the *myo*-inositol ligand and atoms in the IbpA protein.

Phylogenetic tree construction. Six sequences from proteins involved in *myo*-inositol uptake, including *C. crescentus* IbpA (UniProt accession no. B8H228), *Sinorhizobium meliloti* Q926E6, *Mesorhizobium loti* Q98CU7, *Agrobacterium tumefaciens* A9CF36, *Brucella melitensis* Q8YIQ0 (14), and *Pseudomonas* sp. strain GM48 J2ZWP7 (46), and five sequences

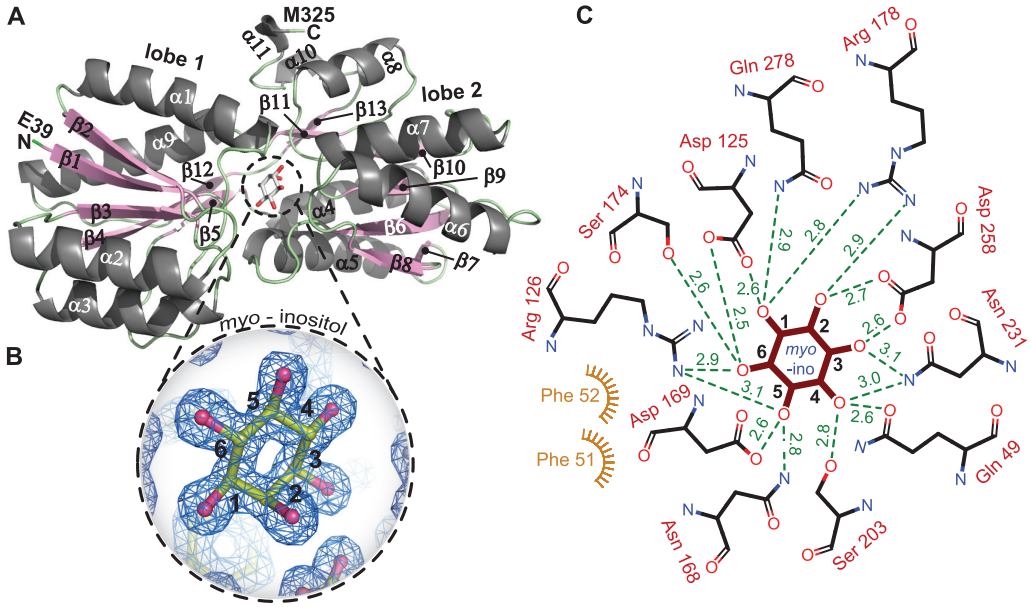

FIG 2 Structure of the IbpA protein bound to *myo*-inositol. (A) Ribbon structure of IbpA. α-Helices (light gray) and β-strands (light pink) are numbered. (B) Simulated annealing composite omit map (contoured at 2σ) of bound *myo*-inositol in the IbpA ligand-binding cavity. (C) Interaction map of the IbpA side chain-ligand interactions in the IbpA/*myo*-inositol structure. Measured distances from side chain nitrogen and oxygen atoms to the hydroxyl oxygens of *myo*-inositol are shown in green. *myo*-Inositol carbons are numbered in panels B and C.

corresponding to PBPs that mediate ribose uptake, including *Escherichia coli* P02925 (47), *Salmonella enterica* serovar Typhimurium F5ZWH0 (48), *Bacillus subtilis* P36949 (49), *Thermoanaerobacter tengcongensis* Q8RD41 (32), and *Thermotoga maritima* Q9X053 (30), were used to construct a BIONJ neighbor-joining phylogenetic tree with the phylogeny.fr suite (50). Xylose-binding proteins from *E. coli* (UniProt accession no. P37387) (51) and *Thermoanaerobacter ethanolicus* (O68456) (52) were used as an outgroup. Evolutionary distances for tree construction were calculated with protdist (53) and the WAG amino acid replacement matrix (54). Bootstrapping was conducted with Seqboot and Consense (number of bootstrap replicates = 100) (53).

Protein structure accession number. Coordinates of *C. crescentus* IbpA have been deposited in the PDB (code 4IRX).

RESULTS

Crystal structure of IBP IbpA. An N-terminally His_6-tagged fusion of *C. crescentus* IbpA from which the first 38 signal peptide amino acids were removed was expressed in *E. coli* and purified by affinity chromatography. His_6-IbpA(39-326), here referred to simply as IbpA, was crystallized in the presence of the *myo* isomer of inositol (*cis*-1,2,3,5-*trans*-4,6-cyclohexanehexol) and formed monoclinic crystals of space group C2 with cell dimensions of 83.1, 34.9, and 181.8 Å (β = 102.6°). There are two molecules of IbpA in the crystal asymmetric unit. Statistics relating to the final refined model are summarized in Table 1. The Ramachandran plot of each monomer in the asymmetric unit reveals two outliers, D169 and D258. The side chain carboxyl of D169 makes direct contact with a hydroxyl group of *myo*-inositol; residue D258 is a Ramachandran outlier across several members of the periplasmic carbohydrate-binding protein family (55). It is not known if atypical backbone geometry at the D258 position has general functional significance in carbohydrate-binding PBPs.

Each IbpA monomer consists of two α-β lobes that surround a three-segment hinge (segment 1, A140 to N142; segment 2, E277 to P280; segment 3, L306 to V309) (Fig. 2A and 3A). The hinged lobes form a deep cleft that constitutes the *myo*-inositol binding cavity (Fig. 2B). Lobe 1 begins with the amino terminus and consists of β-strands 1 to 5 and 12 and α-helices 1 to 3 and 9. Lobe 2 consists of β-strands 6 to 11 and 13 and α-helices 4 to 8, 10, and 11, and ends at the carboxy terminus (Fig. 2A and 3A). The binding cavity for *myo*-inositol is acidic; 11 residues in the ligand-binding cavity make direct contact with the hydroxyl groups of *myo*-inositol, including Q49, D125, and R126 from lobe 1; N168, D169, S174, R178, S203, N231, and D258 from lobe 2; and Q278 of the hinge. *myo*-inositol is flanked by two phenylalanines (F51 and F52) that make van der Waals contact with the ligand (Fig. 2C).

IbpA is structurally homologous to ribose-binding PBPs. We compared the *C. crescentus* IbpA structure to available structures in the PDB by using the Dali server (44). IbpA shares the highest structural similarity (root mean square deviation [RMSD] = 1.03 Å) with the RBP from *T. tengcongensis* (RBP_{Tt}) (32) (PDB code 2IOY; Z score = 38.7); the next highest hit (RMSD = 1.02 Å) is the structure of *E. coli* RBP (33) (PDB code 2DRI; Z score = 37.5). Amino acid sequence alignment and structural alignment of RBP_{Tt} and IbpA revealed a large set of identical residues in the carbohydrate-binding cavity (identity, 32%). Five residues that make direct contact with *myo*-inositol in IbpA differ from residues at the same positions in RBP_{Tt}: Q49 versus N51, N168 versus G169, D169 versus I170, S174 versus A175, and S203 versus F203 (Fig. 3).

Phylogenetic analysis of RBPs and IBPs. To further assess the relationship between RBPs and IBPs, we conducted a phylogenetic analysis of these carbohydrate-binding proteins. Primary sequences of PBPs that have been experimentally classified as ribose or *myo*-inositol binders were used as our analysis set. Six sequences corresponding to PBPs involved in *myo*-inositol uptake, including *C. crescentus* IbpA (UniProt accession no. B8H228), *S. meliloti* (Q926E6), *M. loti* (Q98CU7), *A. tumefaciens* (A9CF36), *B.*

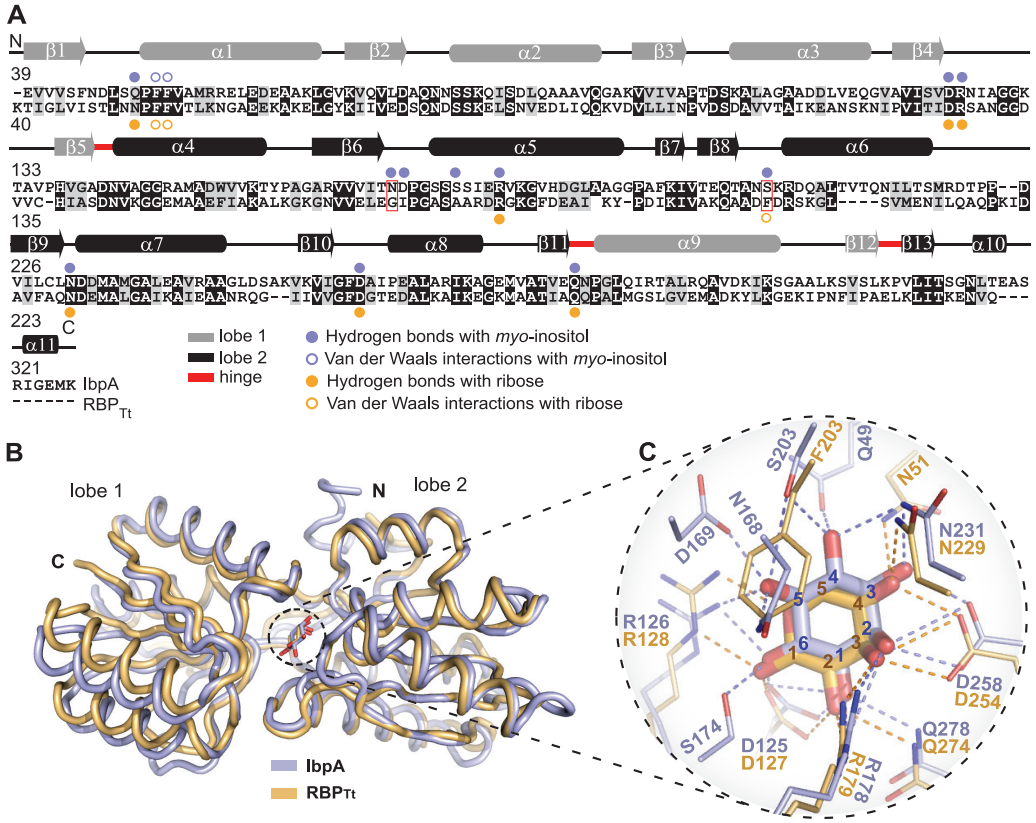

FIG 3 Structural comparison of *C. crescentus* IbpA and *T. tengcongensis* RBP. (A) Amino acid sequence alignment of IbpA (upper sequence) and RBP_{Tt} (lower sequence). Solid and open circles highlight residues involved in polar interactions and hydrophobic interactions, respectively, between IbpA and *myo*-inositol (blue) and between RBP_{Tt} and ribose (orange). Red boxes highlight residues N168 and S203 from IbpA and G169 and F203 from RBP_{Tt} (see Fig. 5). Red lines highlight residues present in the three-segment hinge. α-Helices are represented by cylinders, and β-strands are represented by arrows. The residue at the beginning of each line is numbered. (B) Structural alignment between IbpA (light blue) and RBP_{Tt} (light orange, PDB code 2IOY). RMSD = 1.03 Å. (C) Structural alignment of the binding cavity residues of IbpA (light blue) and RBP_{Tt} (light orange). *myo*-Inositol and D-ribose are in blue and orange, respectively. To improve the visibility of the side chains presented, F51 and F52 in IbpA and F52 and F53 in RBP_{Tt} are not shown. The carbons of each ligand are been numbered in blue for *myo*-inositol and in red for D-ribose.

melitensis (Q8YIQ0) (14), and *Pseudomonas* sp. strain GM48 (J2ZWP7) (46), and five sequences corresponding to PBPs involved in ribose uptake in *E. coli* (UniProt accession no. P02925) (47), *S. enterica* serovar Typhimurium (F5ZWH0) (48), *B. subtilis* (P36949) (49), *T. tengcongensis* (Q8RD41) (32), and *T. maritima* (Q9X053) (30), were aligned in order to calculate evolutionary protein distances and construct a neighbor-joining phylogenetic tree (see Materials and Methods). Xylose-binding proteins from *E. coli* (UniProt accession no. P37387) (51) and *T. ethanolicus* (O68456) (52) were used as an outgroup. *C. crescentus* IbpA occupies an intermediate position on the tree, between RBPs and IBPs (Fig. 4).

IbpA has slightly higher homology to RBP sequences (31% ± 2% identity) than to IBP sequences (27% ± 2% identity). Within their ligand-binding cavities, RBPs and IBPs are similar but can be distinguished at selected positions. The ligand-binding cavity of IbpA has characteristics of an RBP-IBP hybrid. Eleven residues make polar contacts with *myo*-inositol in IbpA, while two phenylalanine residues form packing interactions with ligand-interacting side chains. Certain IbpA residues are more closely related to RBPs in our alignment (e.g., F52 and D125), while others (Q49, N168, D169, and S203) are distinct from the RBP and IBP lineages (Fig. 5A and B). As outlined in the section above, five residues

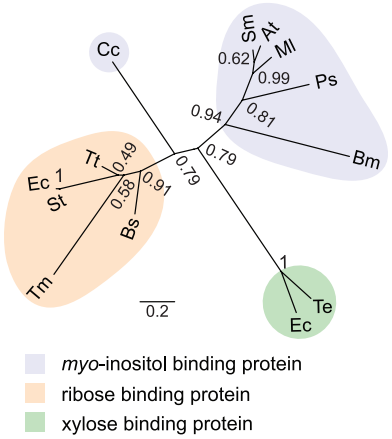

FIG 4 Neighbor-joining phylogenetic tree of IBPs and RBPs. The tree is constructed from six IBP sequences (*C. crescentus* [Cc], *S. meliloti* [Sm], *M. loti* [Ml], *A. tumefaciens* [At], *B. melitensis* [Bm], and *Pseudomonas* sp. strain GM48 [Ps]) and five RBP sequences (*E. coli* [Ec], *S. enterica* serovar Typhimurium [St], *B. subtilis* [Bs], *T. tengcongensis* [Tt], and *T. maritima* [Tm]). Xylose-binding protein sequences from *E. coli* (Ec) and *T. ethanolicus* (Te) are the outgroup. Bootstrap values for 100 replicates are presented at the nodes on the tree.

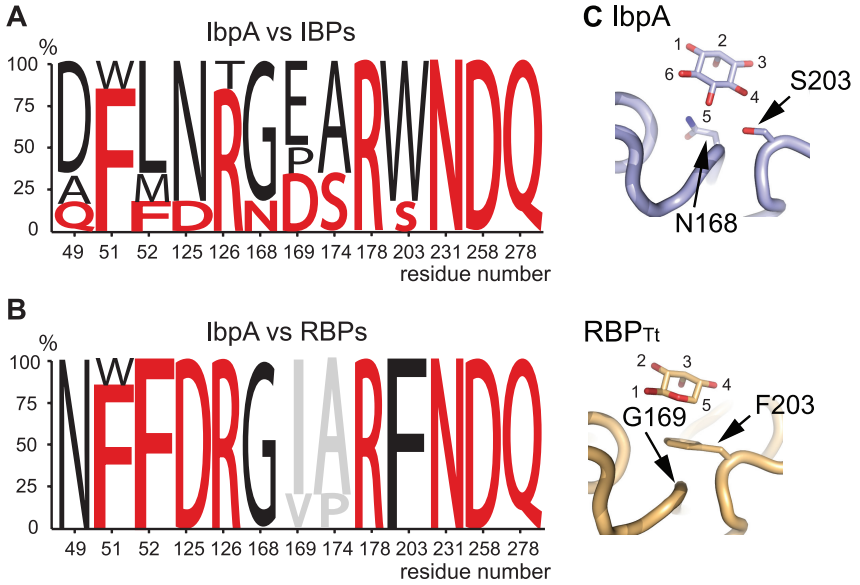

FIG 5 Comparative residue frequencies in the IBP and RBP ligand-binding cavities. Residue numbering is based on the IbpA sequence. For the amino acid sequence alignment used to produce this figure, see Fig. S1 in the supplemental material. (A) Residue frequency in the ligand-binding cavities of IBPs. The residue at each of these positions in *Caulobacter* IbpA is in red. (B) Residue frequency in the ligand-binding cavities of RBPs. The residue at each of these positions in *Caulobacter* IbpA is in red. The residues at positions 169 and 174 are not involved in ligand interaction and are in gray. (C) Spatial organization of the N168-S203 pair in IbpA and the G169-F203 pair in RBP_{Tt} (PDB code 2IOY). *myo*-Inositol and ribose carbons are numbered.

distinguish *C. crescentus* IbpA from RBPs. We note a pair of residues in the ligand-binding cavity (positions 168 and 203) that distinguish IbpA from both RBPs and other IBPs in our alignment (Fig. 5A and B; see Fig. S1 in the supplemental material). IbpA contains a serine at position 203; this serine residue is flanked by asparagine 168. In all other proteins in the alignment, a glycine is present at the position corresponding to N168 and flanks a phenylalanine or a tryptophan at position 203. The Phe residue forms stacking interactions on top of the ribose in RBPs (Fig. 5C). Experiments in which we investigated the functional roles of positions 168 and 203 in ligand binding are described below.

Structure-function analysis of *myo*-inositol and ribose binding to IbpA: an engineered switch in carbohydrate binding specificity. To test the functional roles of specific IbpA residues in binding to carbohydrate ligands, we measured the *myo*-inositol and ribose binding affinities of wild-type and mutant variants of purified IbpA protein by ITC (Fig. 6). Consistent with a role in *myo*-inositol transport, wild-type *C. crescentus* IbpA binds *myo*-inositol with high affinity (0.76 ± 0.08 μM) (Fig. 6A). As discussed above, the binding cavity of IbpA is structurally homologous to RBPs. To assess whether structural homology to RBPs in the ligand-binding cavity is reflected in actual ligand binding function, we also measured the binding of D-ribose to IbpA. IbpA binds D-ribose, albeit with ~70-fold lower affinity (50.8 ± 3.4 μM) than *myo*-inositol (Fig. 6D).

Given that IbpA binds both ribose and *myo*-inositol, we sought to assess the function of residues within the ligand-binding cavity of IbpA in the binding of these carbohydrate ligands. We first introduced mutations into the ligand-binding cavity at four positions that distinguish IbpA from known RBPs: Q49, D169, S174, and S203 (Fig. 5B). These residues were mutated to the most conserved residues in RBPs at the corresponding structural positions (Q49N, D169I, S174A, and S203F; Fig. 5B; see Fig. S1 in the supplemental material) to produce IbpA CM1 ($IbpA_{CM1}$). Though the ligand-binding cavity of mutant $IbpA_{CM1}$ is significantly more closely related to bona fide RBPs, its affinity for ribose is ~6-fold lower (K_d = 289 ± 32 μM) than that of wild-type IbpA. Binding to *myo*-inositol is completely abolished in mutant $IbpA_{CM1}$ (Fig. 6B and E).

We constructed a homology model of $IbpA_{CM1}$ that predicted steric side chain clash between the phenylalanine introduced at position 203 and asparagine 168. All sequences within the RBP clade encode a glycine at position 168 (Fig. 5B; see Fig. S1 in the supplemental material), which allows F203 to enter a stacked conformation with the ribose ring (Fig. 5C). On the basis of these structures, we predicted that the addition of an N168G mutation would alleviate the steric clash with the F203 position and increase the affinity of the mutant protein for a ribose ligand. We thus generated IbpA CM2 ($IbpA_{CM2}$), which contained the mutations Q49N, N168G, D169I, S174A, and S203F. $IbpA_{CM2}$ binds D-ribose with high affinity (4.9 ± 1.2 μM) (Fig. 6F), approximately 60-fold higher than ribose binding to $IbpA_{CM1}$ and 10-fold higher than ribose binding to wild-type IbpA. Like $IbpA_{CM1}$, $IbpA_{CM2}$ does not bind *myo*-inositol (Fig. 6C). Thus, the introduction of five mutations into the ligand-binding cavity of *C. crescentus* IbpA is sufficient to confer a switch in binding specificity from *myo*-inositol to ribose.

As a control to ensure that the changes in ligand binding affinities between wild-type and mutant IbpA proteins were not a result of changes in global protein folding and stability, we measured the UV CD spectra of purified IbpA, $IbpA_{CM1}$, and $IbpA_{CM2}$. Estimation of the α-helix and β-strand contents of each mutant from the UV CD spectra demonstrated that all three proteins have similar α-helix and β-strand contents (average α-helix content, ~34%; average β-strand content, ~17%). These values are con-

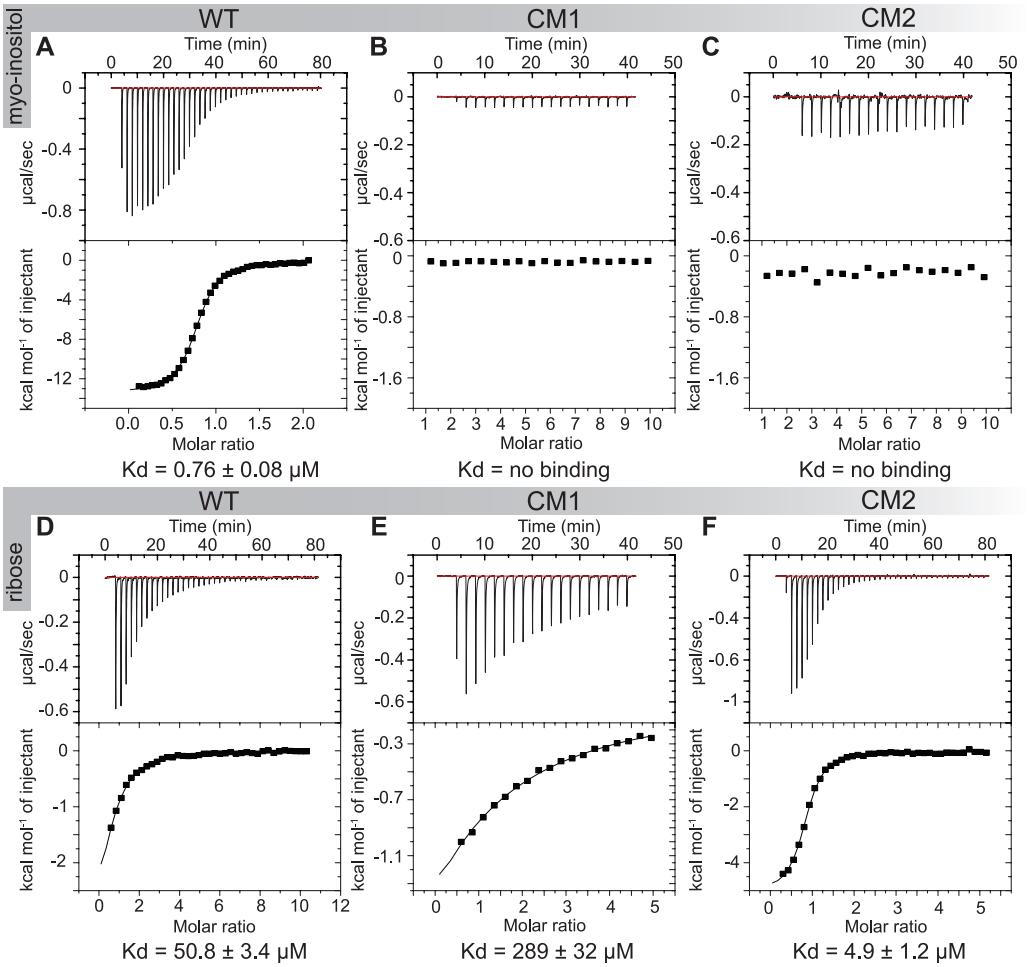

FIG 6 ITC carbohydrate binding assays. In each panel, the raw heat signal is displayed above the integrated and fitted data (below). Equilibrium dissociation constants (K_d values) were calculated for each titration after subtraction of the buffer heat of dilution. (A) Binding interaction between IbpA and *myo*-inositol. WT, wild type. (B) Binding interaction between $IbpA_{CM1}$ and *myo*-inositol. (C) Binding interaction between $IbpA_{CM2}$ and *myo*-inositol. (D) Binding interaction between IbpA and D-ribose. (E) Binding interaction between $IbpA_{CM1}$ and D-ribose. (F) Binding interaction between $IbpA_{CM2}$ and D-ribose.

sistent with the helix and strand contents of the IbpA crystal structure (α-helix content, 44%; β-strand content, 18%) (Fig. 7A).

Functional analysis of wild-type and mutant IbpA in *C. crescentus* cells. We next measured the effect of IbpA ligand-binding cavity mutations on *C. crescentus* cell growth in medium containing either *myo*-inositol or ribose as the sole carbon source. As previously described (14), the growth of *C. crescentus* in M2 defined medium (56) supplemented with 0.2% (wt/vol) *myo*-inosi-

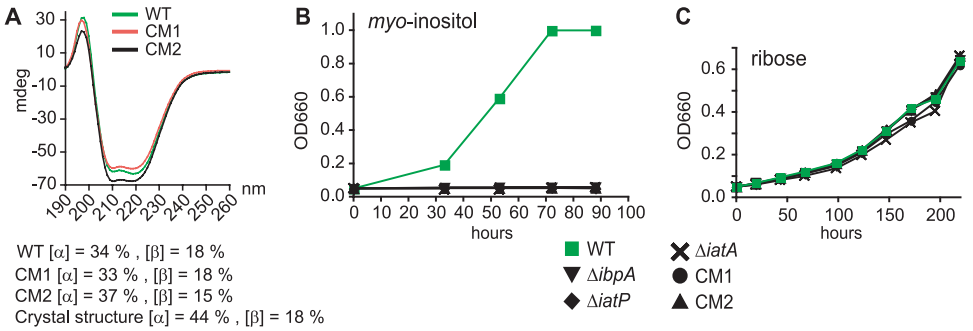

FIG 7 Effects of ABC transporter mutations and IbpA cavity mutations on *C. crescentus* growth on *myo*-inositol and D-ribose. (A) Folding of the different IbpA CMs (CM1 and CM2) was compared to that of the wild-type (WT) protein by UV CD spectroscopy. The α-helix and β-strand contents of each protein were calculated from the CD spectra and compared to the IbpA crystal structure. mdeg, millidegrees. (B) Growth curves of wild-type *C. crescentus*, ABC transporter mutants, and IbpA CMs in M2 defined medium supplemented with 0.2% (wt/vol) *myo*-inositol. (C) Growth curves of wild-type *C. crescentus*, ABC transporter mutants, and IbpA CMs in M2 defined medium supplemented with 0.2% (wt/vol) D-ribose.

tol (M2-inositol) requires each gene of the *myo*-inositol transport system (i.e., *ibpA*, *iatP*, and *iatA*) (Fig. 7B). We performed this same cell growth experiment with M2 defined medium supplemented with 0.2% (wt/vol) D-ribose (M2-ribose). Wild-type *C. crescentus* grows slowly in M2-ribose, with a doubling time of 62 ± 1 h (Fig. 7C). Deletion of *ibpA*, *iatP*, or *iatA* has no effect on cell growth in M2-ribose (Fig. 7C).

To assess the effects of mutations in the IbpA ligand-binding cavity on *C. crescentus* growth in defined medium, we replaced the wild-type chromosomal copy of *ibpA* with either the $ibpA_{CM1}$ or the $ibpA_{CM2}$ allele by double-crossover recombination. Neither the $ibpA_{CM1}$ nor the $ibpA_{CM2}$ allele replacement strain was able to grow in M2-inositol medium (Fig. 7B). This result provides evidence that *C. crescentus* growth on *myo*-inositol as the sole carbon source requires an IbpA allele that is competent to bind *myo*-inositol. We further tested the growth of the $ibpA_{CM1}$ and $ibpA_{CM2}$ allele replacement strains in M2-ribose medium. As expected from the Δ*ibpA* mutant growth experiment, neither the $ibpA_{CM1}$ nor the $ibpA_{CM2}$ mutant had defects in growth on ribose (Fig. 7C).

DISCUSSION

We have solved a high-resolution crystal structure of IbpA bound to *myo*-inositol, which constitutes the first structure of a PBP bound to this class of carbohydrate. A comparison of IbpA to PBP sequences in the nonredundant database of GenBank (57) and to structures in the PDB (58) revealed significant homology between IbpA and RBPs (Fig. 3 to 5). The crystal structure of IbpA thus provides a foundation for comparative analysis of PBPs that bind *myo*-inositol and D-ribose. The phylogenetic, structural, and biochemical analyses presented herein have yielded molecular-level insight into inositol- and ribose-binding specificity in these related classes of ABC transporter PBPs.

IbpA binds *myo*-inositol *in vitro* with an affinity of 0.76 μM, which is consistent with the measured affinities of carbohydrate-binding PBPs, including the *myo*-inositol-binding PBP of *Pseudomonas* sp. (46). As previously described, *ibpA* and the adjacent membrane permease (*iatP*) and ATPase (*iatA*) genes are required for *C. crescentus* growth on *myo*-inositol as the sole carbon and energy source (14). We have shown that IbpA also binds D-ribose with 51 μM affinity and demonstrated that *C. crescentus* will grow slowly on ribose as the sole carbon and energy source. However, genetic perturbation of the IbpA-IatP-IatA *myo*-inositol transporter has no effect on *C. crescentus* growth on D-ribose as the sole carbon and energy source at the assessed ribose concentration of 0.2% (13.3 mM) (Fig. 7C). Thus, the IbpA-IatP-IatA transporter system is apparently not involved in ribose uptake, even though IbpA binds ribose. This result is consistent with the known properties of ABC carbohydrate transporters, which exhibit a high degree of specificity for their transported substrates (1, 2, 59). To date, the system responsible for D-ribose uptake in *C. crescentus* remains undefined.

IbpA binds *myo*-inositol with an affinity approximately 70-fold higher than that for D-ribose (Fig. 6). Previous studies have shown that the specificity and affinity of PBPs for a ligand can be modified by cavity mutagenesis (60–62). Given the sequence and structural homology between IbpA and RBPs, we sought to design a variant of IbpA in which the specificities for *myo*-inositol and D-ribose are switched (i.e., an IbpA mutant that binds ribose with an affinity higher than that for inositol). To this end, we engineered two distinct IbpA CMs, $IbpA_{CM1}$ and $IbpA_{CM2}$. The CM1 mutant protein contains four mutations, Q49N, D169I, S174A, and S203F, that were predicted to increase the affinity of IbpA for D-ribose by modifying the cavity to an RBP-like cavity (32, 33). However, the introduction of these residues did not result in increased affinity of the protein for a ribose ligand. Rather, the affinity of $IbpA_{CM1}$ for ribose was significantly lower than that of the wild-type protein (K_d = 289 μM). We detected no binding interaction between $IbpA_{CM1}$ and *myo*-inositol, providing evidence that these four mutations increase the specificity for ribose relative to that for inositol (though ribose binding affinity was very low).

On the basis of homology modeling, we attributed the lowered ribose binding affinity of $IbpA_{CM1}$ to a steric clash between the introduced side chain of F203 and the side chain of N168 (Fig. 3C and 5C). Substitution of glycine for N168 was predicted to alleviate this steric clash and allow the F203 phenyl ring to align in a parallel conformation with the ribose ring, as observed in RBP crystal structures (Fig. 3C and 5C). We thus engineered CM2 ($IbpA_{CM2}$), which contained the same four mutations described in $IbpA_{CM1}$ plus an N168G mutation. Introduction of N168G increased the affinity of $IbpA_{CM2}$ for D-ribose by ~60-fold relative to that of $IbpA_{CM1}$ and 10-fold relative to that of wild-type IbpA (K_d = 5 μM) (Fig. 6). Like $IbpA_{CM1}$, $IbpA_{CM2}$ could be stably expressed and purified but failed to bind *myo*-inositol *in vitro* (Fig. 6). Thus, a combination of five mutations in the ligand-binding cavity was sufficient to create a variant of IbpA that binds D-ribose with high affinity but does not bind *myo*-inositol. We further assessed the loss of *myo*-inositol binding function in $IbpA_{CM1}$ and $IbpA_{CM2}$ *in vivo*; *C. crescentus* $ibpA_{CM1}$ and $ibpA_{CM2}$ chromosomal allelic-replacement mutants failed to grow on *myo*-inositol as the sole carbon and energy source (Fig. 7B).

The role of residues at IbpA positions 168 and 203 merits further discussion. Classic carbohydrate-binding proteins typically have an aromatic residue (Phe or Trp) at position 203 (Fig. 3 and 5) that makes van der Waals contact with the carbohydrate (30, 32, 51, 63, 64). When Phe or Trp is present at this position, a glycine residue is systematically present at position 168 (Fig. 3 and 5; see Fig. S1 in the supplemental material). Presumably, the absence of a Cβ at position 168 is required for the proper packing of Phe/Trp within the carbohydrate-binding cavity (32, 33). Indeed, experimental data presented in this study reveal a key role for G168 in the designed high-affinity ribose-binding variant $IbpA_{CM2}$, which contains a Phe at position 203 (Fig. 6F). Compared to other IBP and RBP proteins (Fig. 5; see also alignment in Fig. S1), *C. crescentus* IbpA is atypical at positions 203 and 168 as it contains neither an aromatic residue at position 203 nor a glycine at position 168. Rather, the polar S203 and N168 side chains in wild-type IbpA make close hydrogen bonds with adjacent hydroxyl groups of the bound *myo*-inositol ligand (Fig. 2C).

Though the designed $IbpA_{CM2}$ variant matches known RBPs in terms of predicted structural contacts with the ribose ligand (Fig. 3 and 5), the affinity of this mutant with a "ribose-like" cavity is not equivalent to that of bona fide RBP proteins, which have measured ribose binding affinities in the 0.1-to-0.2 μM range (33, 47). This result is consistent with a model in which carbohydrate binding affinity is determined by the additive effects of residues that make direct ligand contacts, as well as residues that indirectly affect ligand cavity side chain conformations and, perhaps, global protein conformational transitions between the open and closed states, as described in maltose-binding protein (65).

In conclusion, *C. crescentus* IbpA presents a case study of a PBP

that is positioned at the phylogenetic intersection of IBPs and RBPs (Fig. 4; see Fig. S1 in the supplemental material). Though IbpA binds both *myo*-inositol and D-ribose *in vitro*, it has no apparent role in ribose utilization in the *C. crescentus* cell, where it specifically functions as the PBP component of an ABC transporter that is required for the utilization of *myo*-inositol as a carbon and energy source (Fig. 7). We have solved a crystal structure of IbpA to 1.45 Å resolution and used the resulting structural model to design an IbpA variant with strongly inverted specificities for inositol and ribose binding. This protein design effort has defined structural determinants of carbohydrate-binding specificity in the related ribose- and *myo*-inositol-binding classes of ABC transporter PBPs.

ACKNOWLEDGMENTS

We thank Elena Solomaha (Chicago Biophysics Core) for assistance with ITC and Heather Pinkett (Northwestern University) for helpful discussion. We thank Jon Henry for providing a whisker from Midnight the cat.

The Advanced Photon Source is supported by the Department of Energy Office of Basic Energy Sciences (contract DE-AC02-06CH11357). The Life Sciences Collaborative Access Team is supported by the Michigan Economic Development Corporation and the Michigan Technology Tri-Corridor (grant 085P1000817).

REFERENCES

1. **Nikaido H, Hall JA.** 1998. Overview of bacterial ABC transporters. Methods Enzymol. **292**:3–20.
2. **Rees DC, Johnson E, Lewinson O.** 2009. ABC transporters: the power to change. Nat. Rev. Mol. Cell Biol. **10**:218–227.
3. **Fischer M, Zhang QY, Hubbard RE, Thomas GH.** 2010. Caught in a TRAP: substrate-binding proteins in secondary transport. Trends Microbiol. **18**:471–478.
4. **Rabus R, Jack DL, Kelly DJ, Saier MH, Jr.** 1999. TRAP transporters: an ancient family of extracytoplasmic solute-receptor-dependent secondary active transporters. Microbiology **145**(Pt 12):3431–3445.
5. **Winnen B, Hvorup RN, Saier MH, Jr.** 2003. The tripartite tricarboxylate transporter (TTT) family. Res. Microbiol. **154**:457–465.
6. **Berntsson RP, Smits SH, Schmitt L, Slotboom DJ, Poolman B.** 2010. A structural classification of substrate-binding proteins. FEBS Lett. **584**: 2606–2617.
7. **Saier MH, Jr.** 2000. A functional-phylogenetic classification system for transmembrane solute transporters. Microbiol. Mol. Biol. Rev. **64**:354–411.
8. **Felder CB, Graul RC, Lee AY, Merkle HP, Sadee W.** 1999. The Venus flytrap of periplasmic binding proteins: an ancient protein module present in multiple drug receptors. AAPS PharmSci. **1**:E2. doi:10.1208/ps010202.
9. **Tam R, Saier MH, Jr.** 1993. Structural, functional, and evolutionary relationships among extracellular solute-binding receptors of bacteria. Microbiol. Rev. **57**:320–346.
10. **Wadhams GH, Armitage JP.** 2004. Making sense of it all: bacterial chemotaxis. Nat. Rev. Mol. Cell Biol. **5**:1024–1037.
11. **Ng WL, Bassler BL.** 2009. Bacterial quorum-sensing network architectures. Annu. Rev. Genet. **43**:197–222.
12. **Jacob-Dubuisson F, Wintjens R, Herrou J, Dupré E, Antoine R.** 2012. BvgS of pathogenic Bordetellae: a paradigm for sensor-kinases with Venus flytrap perception domains. *In* Gross R, Beier D (ed), Two-component systems in bacteria. Caister Academic Press, Würzburg, Germany.
13. **Lolkema JS, Poolman B, Konings WN.** 1998. Bacterial solute uptake and efflux systems. Curr. Opin. Microbiol. **1**:248–253.
14. **Boutte CC, Srinivasan BS, Flannick JA, Novak AF, Martens AT, Batzoglou S, Viollier PH, Crosson S.** 2008. Genetic and computational identification of a conserved bacterial metabolic module. PLoS Genet. **4**:e1000310. doi:10.1371/journal.pgen.1000310.
15. **Galbraith MP, Feng SF, Borneman J, Triplett EW, de Bruijn FJ, Rossbach S.** 1998. A functional *myo*-inositol catabolism pathway is essential for rhizopine utilization by *Sinorhizobium meliloti*. Microbiology **144**: 2915–2924.
16. **Roberts MF.** 2006. Inositol in bacteria and archaea, p 103–104. *In* Majumder AL, Biswas BB (ed), Biology of inositols and phosphoinositides, vol 39. Springer, New York, NY.
17. **Berman T, Magasanik B.** 1966. The pathway of *myo*-inositol degradation in *Aerobacter aerogenes*. Ring scission. J. Biol. Chem. **241**:807–813.
18. **Kawsar HI, Ohtani K, Okumura K, Hayashi H, Shimizu T.** 2004. Organization and transcriptional regulation of *myo*-inositol operon in *Clostridium perfringens*. FEMS Microbiol. Lett. **235**:289–295.
19. **Krings E, Krumbach K, Bathe B, Kelle R, Wendisch VF, Sahm H, Eggeling L.** 2006. Characterization of *myo*-inositol utilization by *Corynebacterium glutamicum*: the stimulon, identification of transporters, and influence on L-lysine formation. J. Bacteriol. **188**:8054–8061.
20. **Poole PS, Blyth A, Reid CJ, Walters K.** 1994. myo-Inositol catabolism and catabolite regulation in *Rhizobium leguminosarum* bv. *viciae*. Microbiology **140**:2787–2795.
21. **Yoshida KI, Aoyama D, Ishio I, Shibayama T, Fujita Y.** 1997. Organization and transcription of the *myo*-inositol operon, *iol*, of *Bacillus subtilis*. J. Bacteriol. **179**:4591–4598.
22. **Mullaney EJ, Daly CB, Ullah AHJ.** 2000. Advances in phytase research. Adv. Appl. Microbiol. **47**:157–199.
23. **Turner BL, Paphazy MJ, Haygarth PM, McKelvie ID.** 2002. Inositol phosphates in the environment. Philos. Trans. R. Soc. Lond. B Biol. Sci. **357**:449–469.
24. **Anderson WA, Magasanik B.** 1971. The pathway of *myo*-inositol degradation in *Aerobacter aerogenes*. Conversion of 2-deoxy-5-keto-D-gluconic acid to glycolytic intermediates. J. Biol. Chem. **246**:5662–5675.
25. **Anderson WA, Magasanik B.** 1971. The pathway of *myo*-inositol degradation in *Aerobacter aerogenes*. Identification of the intermediate 2-deoxy-5-keto-D-gluconic acid. J. Biol. Chem. **246**:5653–5661.
26. **Berman T, Magasanik B.** 1966. The pathway of *myo*-inositol degradation in *Aerobacter aerogenes*. Dehydrogenation and dehydration. J. Biol. Chem. **241**:800–806.
27. **Yoshida K, Yamaguchi M, Morinaga T, Kinehara M, Ikeuchi M, Ashida H, Fujita Y.** 2008. *myo*-Inositol catabolism in *Bacillus subtilis*. J. Biol. Chem. **283**:10415–10424.
28. **Kohler PR, Choong EL, Rossbach S.** 2011. The RpiR-like repressor IolR regulates inositol catabolism in *Sinorhizobium meliloti*. J. Bacteriol. **193**: 5155–5163.
29. **Fukami-Kobayashi K, Tateno Y, Nishikawa K.** 1999. Domain dislocation: a change of core structure in periplasmic binding proteins in their evolutionary history. J. Mol. Biol. **286**:279–290.
30. **Cuneo MJ, Beese LS, Hellinga HW.** 2008. Ligand-induced conformational changes in a thermophilic ribose-binding protein. BMC Struct. Biol. **8**:50. doi:10.1186/1472-6807-8-50.
31. **Björkman AJ, Mowbray SL.** 1998. Multiple open forms of ribose-binding protein trace the path of its conformational change. J. Mol. Biol. **279**:651–664.
32. **Cuneo MJ, Tian Y, Allert M, Hellinga HW.** 2008. The backbone structure of the thermophilic *Thermoanaerobacter tengcongensis* ribose binding protein is essentially identical to its mesophilic *E. coli* homolog. BMC Struct. Biol. **8**:20. doi:10.1186/1472-6807-8-20.
33. **Björkman AJ, Binnie RA, Zhang H, Cole LB, Hermodson MA, Mowbray SL.** 1994. Probing protein-protein interactions. The ribose-binding protein in bacterial transport and chemotaxis. J. Biol. Chem. **269**:30206–30211.
34. **Doublié S.** 2007. Production of selenomethionyl proteins in prokaryotic and eukaryotic expression systems. Methods Mol. Biol. **363**:91–108.
35. **Otwinowski Z, Minor W.** 1997. Processing of X-ray diffraction data collected in oscillation mode. Methods Enzymol. **276**:307–326.
36. **Dauter Z.** 2002. One-and-a-half wavelength approach. Acta Crystallogr. D Biol. Crystallogr. **58**:1958–1967.
37. **Adams PD, Afonine PV, Bunkoczi G, Chen VB, Davis IW, Echols N, Headd JJ, Hung LW, Kapral GJ, Grosse-Kunstleve RW, McCoy AJ, Moriarty NW, Oeffner R, Read RJ, Richardson DC, Richardson JS, Terwilliger TC, Zwart PH.** 2010. PHENIX: a comprehensive Python-based system for macromolecular structure solution. Acta Crystallogr. D Biol. Crystallogr. **66**:213–221.
38. **Emsley P, Cowtan K.** 2004. Coot: model-building tools for molecular graphics. Acta Crystallogr. D Biol. Crystallogr. **60**:2126–2132.
39. **Marks ME, Castro-Rojas CM, Teiling C, Du L, Kapatral V, Walunas TL, Crosson S.** 2010. The genetic basis of laboratory adaptation in *Caulobacter crescentus*. J. Bacteriol. **192**:3678–3688.
40. **Ried JL, Collmer A.** 1987. An *nptI-sacB-sacR* cartridge for constructing

directed, unmarked mutations in gram-negative bacteria by marker exchange-eviction mutagenesis. Gene **57**:239–246.
41. **Fiebig A, Castro Rojas CM, Siegal-Gaskins D, Crosson S.** 2010. Interaction specificity, toxicity and regulation of a paralogous set of ParE/RelE-family toxin-antitoxin systems. Mol. Microbiol. **77**:236–251.
42. **Miller DM, III, Olson JS, Pflugrath JW, Quiocho FA.** 1983. Rates of ligand binding to periplasmic proteins involved in bacterial transport and chemotaxis. J. Biol. Chem. **258**:13665–13672.
43. **Louis-Jeune C, Andrade-Navarro MA, Perez-Iratxeta C.** 2012. Prediction of protein secondary structure from circular dichroism using theoretically derived spectra. Proteins **80**:374–381.
44. **Holm L, Rosenstrom P.** 2010. Dali server: conservation mapping in 3D. Nucleic Acids Res. **38**:W545–549.
45. **Larkin MA, Blackshields G, Brown NP, Chenna R, McGettigan PA, McWilliam H, Valentin F, Wallace IM, Wilm A, Lopez R, Thompson JD, Gibson TJ, Higgins DG.** 2007. Clustal W and Clustal X version 2.0. Bioinformatics **23**:2947–2948.
46. **Deshusses J, Belet M.** 1984. Purification and properties of the *myo*-inositol-binding protein from a *Pseudomonas* sp. J. Bacteriol. **159**:179–183.
47. **Willis RC, Furlong CE.** 1974. Purification and properties of a ribose-binding protein from Escherichia coli. J. Biol. Chem. **249**:6926–6929.
48. **Aksamit RR, Koshland DE, Jr.** 1974. Identification of the ribose binding protein as the receptor for ribose chemotaxis in *Salmonella typhimurium*. Biochemistry **13**:4473–4478.
49. **Woodson K, Devine KM.** 1994. Analysis of a ribose transport operon from Bacillus subtilis. Microbiology **140**(Pt 8):1829–1838.
50. **Dereeper A, Guignon V, Blanc G, Audic S, Buffet S, Chevenet F, Dufayard JF, Guindon S, Lefort V, Lescot M, Claverie JM, Gascuel O.** 2008. Phylogeny.fr: robust phylogenetic analysis for the non-specialist. Nucleic Acids Res. **36**:W465–469.
51. **Sooriyaarachchi S, Ubhayasekera W, Park C, Mowbray SL.** 2010. Conformational changes and ligand recognition of *Escherichia coli* D-xylose binding protein revealed. J. Mol. Biol. **402**:657–668.
52. **Erbeznik M, Strobel HJ, Dawson KA, Jones CR.** 1998. The D-xylose-binding protein, XylF, from *Thermoanaerobacter ethanolicus* 39E: cloning, molecular analysis, and expression of the structural gene. J. Bacteriol. **180**:3570–3577.
53. **Felsenstein J.** 1989. PHYLIP—phylogeny inference package (version 3.2). Cladistics **5**:164–166.
54. **Whelan S, Goldman N.** 2001. A general empirical model of protein evolution derived from multiple protein families using a maximum-likelihood approach. Mol. Biol. Evol. **18**:691–699.
55. **Magnusson U, Chaudhuri BN, Ko J, Park C, Jones TA, Mowbray SL.** 2002. Hinge-bending motion of D-allose-binding protein from *Escherichia coli*: three open conformations. J. Biol. Chem. **277**:14077–14084.
56. **Ely B.** 1991. Genetics of *Caulobacter crescentus*. Methods Enzymol. **204**:372–384.
57. **Benson DA, Karsch-Mizrachi I, Clark K, Lipman DJ, Ostell J, Sayers EW.** 2012. GenBank. Nucleic Acids Res. **40**:D48–D53.
58. **Berman HM, Westbrook J, Feng Z, Gilliland G, Bhat TN, Weissig H, Shindyalov IN, Bourne PE.** 2000. The Protein Data Bank. Nucleic Acids Res. **28**:235–242.
59. **Saier MH, Jr.** 2000. Families of transmembrane sugar transport proteins. Mol. Microbiol. **35**:699–710.
60. **Sakaguchi-Mikami A, Taneoka A, Yamoto R, Ferri S, Sode K.** 2008. Engineering of ligand specificity of periplasmic binding protein for glucose sensing. Biotechnol. Lett. **30**:1453–1460.
61. **Looger LL, Dwyer MA, Smith JJ, Hellinga HW.** 2003. Computational design of receptor and sensor proteins with novel functions. Nature **423**:185–190.
62. **Jeffery CJ.** 2011. Engineering periplasmic ligand binding proteins as glucose nanosensors. Nano Rev. **2**:5743. http://www.ncbi.nlm.nih.gov/pmc/articles/PMC3215197/pdf/NANO-2-5743.pdf.
63. **Chaudhuri BN, Ko J, Park C, Jones TA, Mowbray SL.** 1999. Structure of D-allose binding protein from *Escherichia coli* bound to D-allose at 1.8 A resolution. J. Mol. Biol. **286**:1519–1531.
64. **Zou JY, Flocco MM, Mowbray SL.** 1993. The 1.7 Å refined X-ray structure of the periplasmic glucose/galactose receptor from *Salmonella typhimurium*. J. Mol. Biol. **233**:739–752.
65. **Marvin JS, Hellinga HW.** 2001. Manipulation of ligand binding affinity by exploitation of conformational coupling. Nat. Struct. Biol. **8**:795–798.